Science
AAAS

Supplementary Materials for

Super-nano domains enable strength-conductivity synergy in copper foils

Zhao Cheng *et al*.

Corresponding author: Lei Lu, llu@imr.ac.cn

Science **392**, 275 (2026)
DOI: 10.1126/science.aed7758

The PDF file includes:

Materials and Methods
Figs. S1 to S11
Table S1
References

Materials and methods

Materials

The periodically distributed super-nano domain (GSD) Cu foils were synthesized using a direct-current electrodeposition technique in an electrolyte of 200 g/L $CuSO_4$ adjusted to a pH value of ~1 with H_2SO_4. A Ti rod (90 mm in diameter and 80 mm in height) served as the cathode, producing as-deposited Cu foils with the in-plane dimensions of 280 × 80 mm^2. The Ti cathode was mechanically polished to minor surface roughness and rotated at 500 rpm during deposition. An Ir-Ta-coated Ti pipe, with a diameter twice that of the Ti cathode and of equal height, was used as the anode. Both electrodes were positioned coaxially. Electrodeposition was performed at ~30 °C under a constant current density of 650 mA/cm^2. Each deposition lasted ~55 s, yielding a Cu foil ~10 μm thick. During deposition, a composite additive consisting of gelatin, hydroxyethyl cellulose (HEC), and 2-mercaptobenzimidazole (MBI) with their mass ratio of 4:2:1, along with KCl, was used to prepare the GSD Cu foils. GSD Cu foils with structural gradients of 42, 68 and 113 μm^{-1} were prepared by increasing the total composite additive concentration to 25, 30, and 35 mg/L, respectively, while maintaining a constant KCl concentration of 45 mg/L. After deposition, the Cu foils were peeled off from the cathode. All chemicals used in the virgin make-up solution (VMS) and the additives were analytical-reagent (AR) grade and were purchased from Sinopharm Chemical Reagent Co., Ltd.

For comparison, randomly distributed domain (RD) Cu foils were electrodeposited using the composite additive concentration of 25 mg/L but at a higher current density of 800 mA/cm^2, with all other parameters identical to those for GSD Cu foils. Conventional nanograined (NG) Cu foils were prepared using a commercial electrodeposition additive, while keeping all other parameters consistent with those of the GSD Cu foils.

The roles of individual components in the composite additive are well established in the literature. HEC acts as a surfactant that facilitates the removal of evolved hydrogen, particularly at high current densities (*51*). Gelatin and MBI function as inhibitors, increasing the resistance to Cu^{2+} reduction via their -NH_2 and -SH functional groups, respectively (*7, 52*). Both additives promote grain refinement by increasing the deposition overpotential. However, the overpotential generated by a single additive tends to saturate as its concentration increases. In this study, we combine additives of gelatin and MBI, which can produce a substantially higher and more sustained overpotential. This enhanced overpotential promotes their co-deposition with Cu^{2+}, leading to the formation of super-nano domains through the incorporation of organic elements into a solid solution. In contrast, chlorine ions (Cl^-) accelerate Cu^{2+} reduction and lower the overpotential, thereby exerting an antagonistic effect. This competition induces oscillations in electrical potential at the cathode surface, which in turn drive the periodic formation of super-nano domain rich and lean nanolayers, as discussed below.

Under the high applied current density used in this study, the deposition process becomes diffusion-limited. Specifically, owing to their larger molecular size, the organic additives diffuse more slowly than Cl^- and Cu^{2+} ions. When sufficient additives accumulate at the cathode surface, a high overpotential develops, promoting co-deposition and the formation of a domain-rich layer II. As these accumulated additives are consumed, the antagonistic effect of Cl^- lowers the overpotential, suppressing domain formation and resulting in a domain-lean Cu layer I. This cyclical accumulation of additive accumulation and depletion at the cathode surface repeats during deposition, giving rise to the observed periodic alternation between layer I and layer II.

As discussed above, the periodicity of super-nano domains arises from the interplay among the composite additive components and does not require external pulsing of current or voltage. The characteristic accumulation wavelength, comprising alternating domain-lean layer I and domain-rich layer II, is governed by the rate at which additives accumulate at the cathode.

Our study demonstrates that additive concentration and current density are the key parameters controlling the periodicity of super-nano domains. For example, in GSD-42, the lower additive concentration (25 mg/L) leads to a slower accumulation rate. This condition requires a longer time to reach the threshold concentration needed to generate the high overpotential for super-nano domain formation. As a result, a larger wavelength of ~150 nm is observed. Increasing the additive concentration to 35 mg/L (GSD-113) accelerates additive accumulation, thereby reducing the wavelength to ~120 nm.

Furthermore, the applied current density of 650 mA/cm^2 is critical for establishing the periodic arrangement of super-nano domains in GSD Cu foils. In contrast, an excessively high current density (e.g., 800 mA/cm^2) disrupts this periodicity, producing a random distribution of super-nano domains throughout the foil thickness and resulting in a uniform domain structure. This loss of modulation occurs because the enhanced electrochemical polarization at 800 mA/cm^2 overwhelms the antagonistic effect of chloride ions, enabling continuous co-deposition of organic additives and thus uninterrupted formation of super-nano domains.

Chemical analysis

Chemical composition analysis was conducted using time-of-flight secondary ion mass spectrometry (ToF-SIMS, ION TOF-SIMS 5). TOF-SIMS imaging was performed with a Bi^+ primary ion beam operated at an acceleration voltage of 30 keV and a beam current of 1.0 pA. During depth profiling, a Cs^+ ion gun was operated at 2 keV and 60 nA for sputtering to remove the surface layers of the Cu foils, creating a crater measuring 300×300 μm^2 with a final depth exceeding 3 μm, as determined using a KLA-Tencor profilometer. Chemical analysis was carried out in a 100×100 μm^2 area located at the center of the sputtered crater. Effective data acquisition began after ~10 s of sputtering, once the surface contamination was removed. While the instrument provides an in-plane resolution of ~50 nm, its depth resolution reaches ~1 nm, which is sufficient to resolve the periodic fluctuations of impurity elements along the thickness of GSD Cu foil. These fluctuations exhibit a characteristic length scale of ~120 nm in GSD-113. In contrast, TOF-SIMS depth profiling of the RD Cu foil, which contains random super-nano domains, reveals a largely homogeneous element distribution (Fig. S1D), unlike the periodic variation observed in GSD-113 (Fig. S1C).

Quantitative chemical composition of the as-deposited Cu foil was further analyzed using a glow discharge mass spectrometer (GDMS, ASTRUM). The GDMS measurements were conducted with a direct current voltage of 1000 V and a stabilized discharge current of 1.5 mA. The analysis chamber was maintained at approximately −160 °C using a liquid nitrogen cooling system to minimize background interference and enhance signal stability. Prior to data collection, a pre-sputtering step was applied to remove surface contaminants and achieve steady-state sputtering conditions.

Electrochemical analysis

Electrochemical analysis on the process of GSD and RD Cu foils was carried out in an electrochemical three electrode cell by using a Vionic workstation. A rotating disk electrode test system was used for electrochemical tests from the Metrohm Autolab with an auto-lab RDE working electrode with 5-mm diameter, while a platinum plate with diameter of 3 cm and an Ag/AgCl electrode in a saturated KCl solution were used as counter electrode and reference electrode, respectively. A jacketed beaker was connected to a circulating water bath to stabilize the temperature at about 30 °C during all electrochemical experiments. Linear sweep voltammetry (galvanostatic) procedures of GSD and RD Cu foils were carried out to monitor the evolution of voltage at their respective deposition parameters for 40 s.

Microstructure characterization

Cross-sectional microstructures of the as-deposited and deformed GSD Cu foils were characterized using an FEI NovaSEM 460 field emission SEM in backscattering electron (BSE) mode. The average grain size was obtained from SEM images by measuring over 500 grains for each GSD Cu foil. Prior to SEM observation, samples were electrochemically polished in a solution of phosphoric acid (25%), alcohol (25%), and deionized water (50%) at ambient temperature.

A dual-beam focused ion beam (FIB) system (Helios G4 CX, Thermo Fisher Scientific) equipped with a gallium ion source was used to prepare cross-sectional specimens for further microstructural characterization. Crystallographic orientation and texture of the FIB-prepared samples were examined using a Transmission Kikuchi Diffraction (TKD, Oxford Aztec). TKD data were acquired at an accelerating voltage of 30 kV, a working distance of 4 mm, and a sample tilt of -20°.

Cross-sectional microstructural and compositional analyses of the as-deposited and deformed GSD Cu foils were performed using transmission electron microscopy (TEM, Talos F200s, 200 kV). High-angle annular dark field (HAADF) imaging, sensitive to atomic number (*Z*) contrast, was employed to identify super-nano domains appearing as darker contrasts within the Cu matrix. The volume fraction of domains (*f*) at each depth was calculated using the relation $f = \frac{\pi d_D^3}{6l^3}$, where d_D and l are the domain size and spacing, respectively. The overall f value corresponds to the average across both layers I and II, while the structural gradient of the GSD is defined as the slope of f with respect to depth.

The spatial distribution of super-nano domains was reconstructed by 3D tomography with sample tilts ranging from -60° to +60° with 3° increment. STEM bright-field (STEM-BF) imaging along the [110] zone axis under two-beam conditions with a diffraction vector of ***g* = -111** was used to characterize dislocation morphologies in deformed GSD Cu foils. This imaging condition enhances sensitivity to lattice defects while minimizing bend-contour artifacts, thereby improving the reliability of dislocation analysis (*53*). The Burgers vectors (**b**) of dislocations were determined using standard **g·b** analysis, and the dislocation density was quantified by counting dislocation lines per unit area in TEM images.

Atomic-resolution HAADF and integrated differential phase contrast (iDPC) imaging were conducted using an aberration-corrected TEM (Themis Z, 300 kV, Thermo Fisher Scientific) to reveal the atomic core structure of super-nano domains. The HAADF collection semi-angle was set between 60-200 mrad. To further resolve super-nano domains, off-axis HAADF and iDPC imaging (beam tilts of ~30–35 mrad) were conducted to suppress channeling effects in the Cu matrix. This approach improved contrast between super-nano domains and the thicker (>30 nm) matrix, producing clear lattice fringes and enabling reliable identification of dislocations at super-nano domain/matrix interfaces.

Micro-hardness measurements

Cross-sectional micro-hardness measurements were performed using a QnessQ10A+ micro-hardness tester with a load of 5 g and a loading time of 5 s. For each sample, 10 to 20 independent measurements were conducted to ensure statistical reliability.

Uniaxial tensile tests

Uniaxial tensile tests of the GSD Cu foils were conducted in accordance with the IPC-TM-650 standard. The as-deposited foils were cut into rectangular specimens measuring 150 mm in length and 12.7 mm in width by using a precision cutting tool (JDC-0.5-10). The specimen thickness was measured by a weighting method following the IPC-TM-650 standard. Tensile tests were performed on an Instron 68TM-5 microtester at room temperature. The gauge length and crosshead speed were set to 50 mm and 50 mm/min, respectively. To ensure reproducibility, 6 independent tensile tests were carried out for each type of specimens, and the average values and standard deviations of ultimate tensile strength and uniform elongation were calculated.

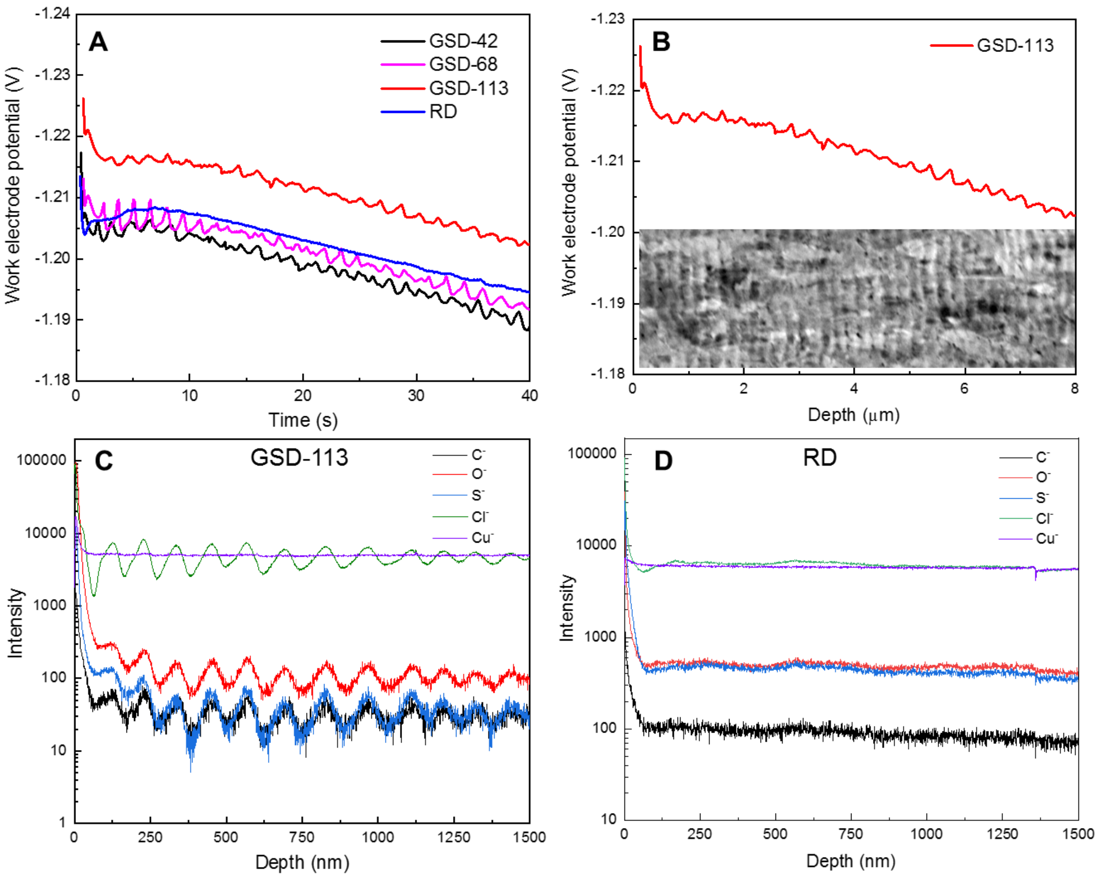

Fig. S1 (A) Galvanostatic polarization curves of the working electrode during the preparation of GSD and RD Cu foils. (B) Periodic fluctuations in the electrode potential with depth (thickness) closely correspond to the spatial periodicity of the super-nano domain structure in GSD-113. (C) GSD-113 shows clear periodic fluctuations of C, O, S and Cl along the depth direction. (D) In contrast, the RD Cu foil exhibits a homogeneous distribution of all elements.

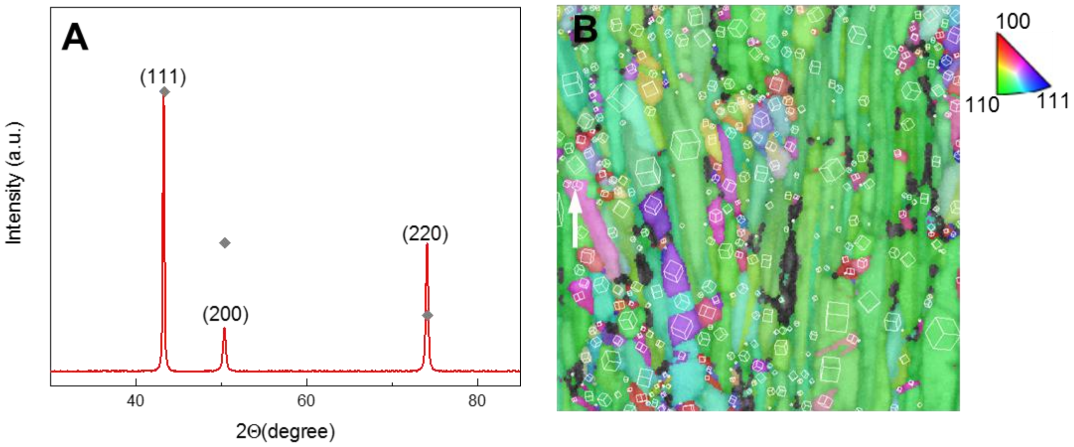

Fig. S2 (A) X-Ray diffraction (XRD) pattern of GSD-113 specimen shows the stronger (220) diffraction peak compared to the standard powder diffraction file of Cu (indicated by grey rhombus) where both (111) peak intensities are normalized. (B) EBSD orientation map collected using transmission Kikuchi diffraction (TKD) in SEM, showing columnar grains with a predominant <110> orientation along the thickness of GSD-113.

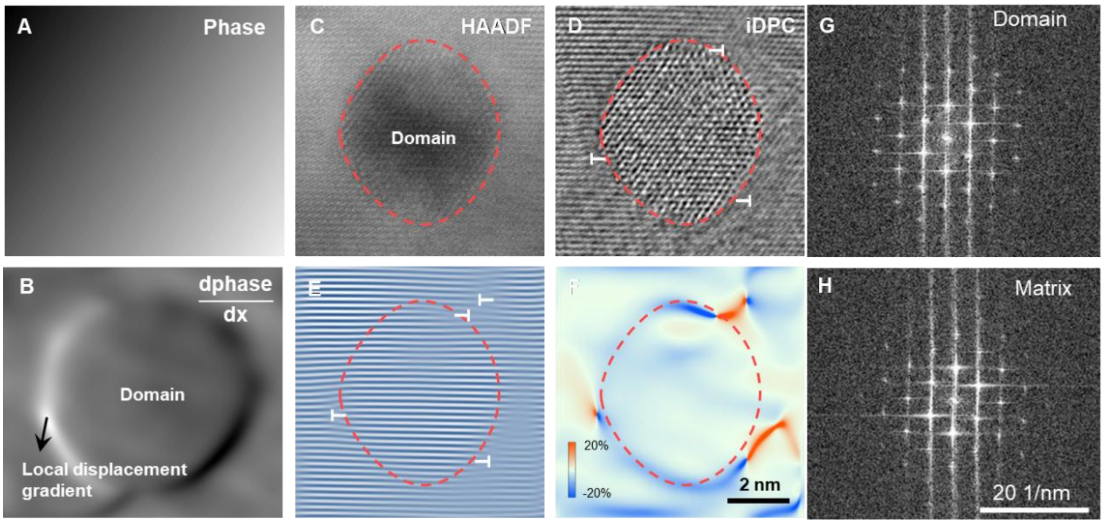

Fig. S3 (A) Phase image reconstructed from the diffraction spot of a selected domain in the GSD-113 sample using geometric phase analysis (GPA) of the high-resolution image in Fig. 1F. (B) The corresponding phase-gradient (dφ/dx) map reveals localized lattice displacements concentrated at the domain–matrix interface. (C, D) Off-axis HAADF and iDPC images reveal interfacial dislocations, marked by dislocation symbols (⊥). (E, F) Inverse FFT filtering of the selected reflection and GPA-derived strain mapping (ε_{yy}) further emphasize localized interfacial strain fields associated with these dislocations. (A-F) share the same scale bar (2 nm). Fast Fourier transformation (FFT) images reveal the diffraction pattern of super-nano domain (G) similar to that of the neighboring matrix (H).

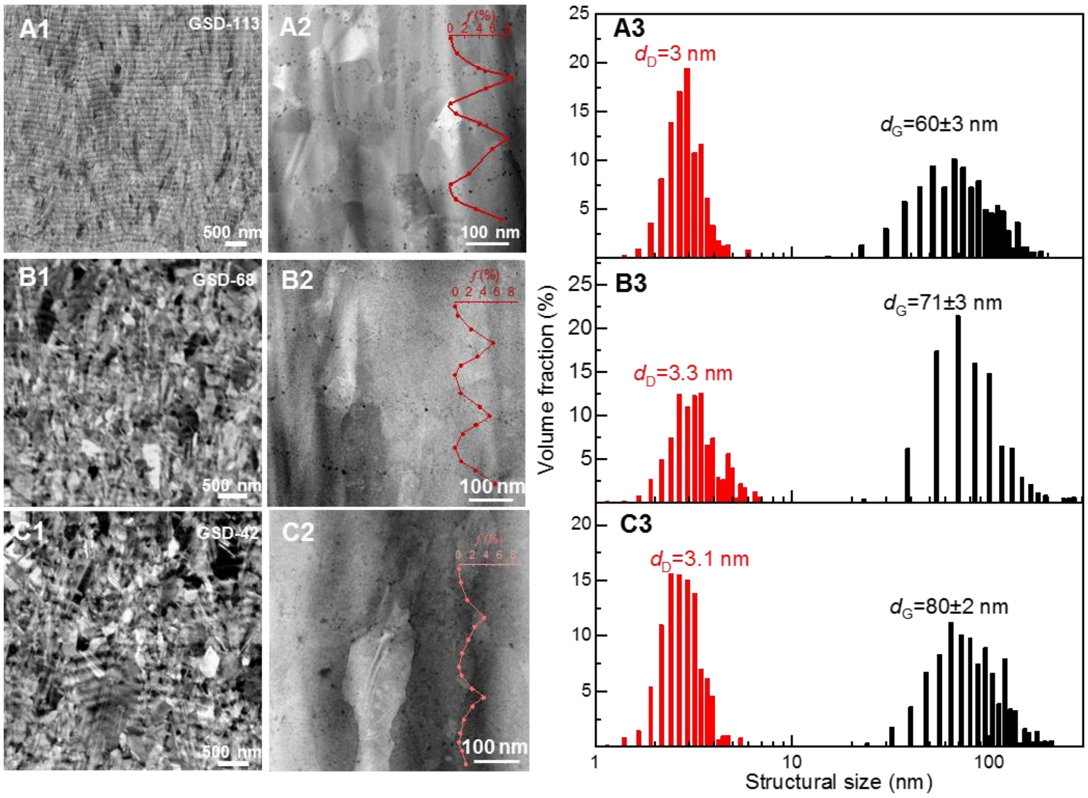

Fig. S4 (A1) Cross-sectional SEM-BSE image, (A2) HAADF image, and (A3) quantitative distributions of grain size (d_G) and domain size (d_D) distributions for the GSD-113 sample. The inset in (A2) shows the variation of precipitate volume fraction along the foil depth. (B1–B3) and (C1–C3) present corresponding structural and statistical analyses for the GSD-68 and GSD-42 samples, respectively.

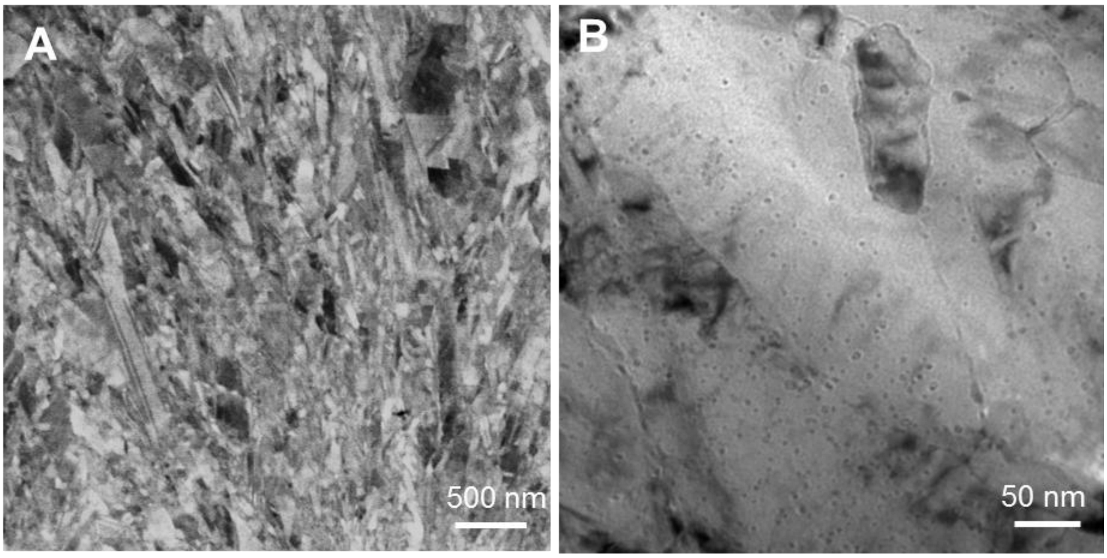

Fig. S5 Cross-sectional SEM-BSE image (A), and TEM image (B) of the RD Cu foils, showing randomly distributed domains throughout the film thickness.

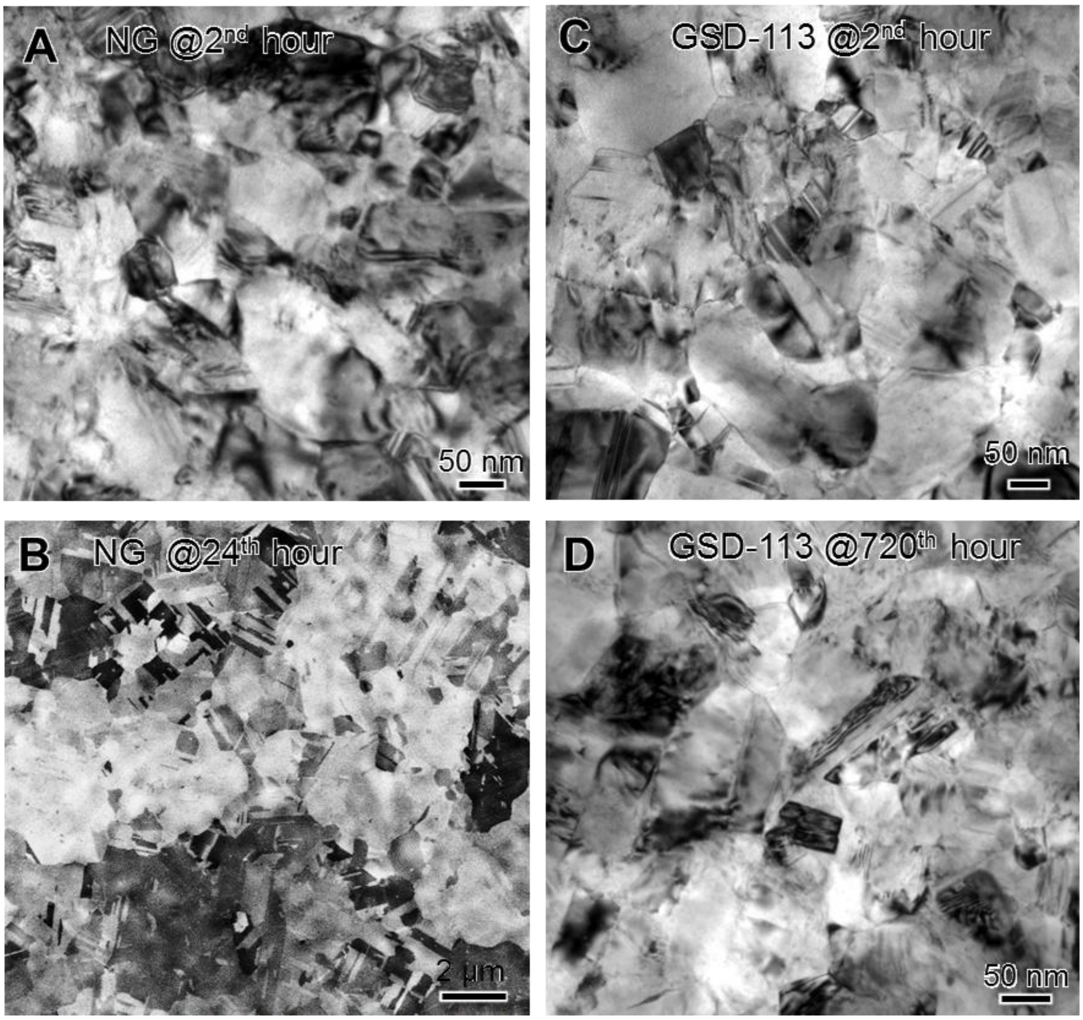

Fig. S6 Plan-view TEM image (A) of a conventional NG Cu foil after 2 hours and SEM image (B) of the same sample after a 24-hour relaxation period. (C and D) Plan-view TEM images of a GSD-113 foil after durations of 2 and 720 hours, respectively.

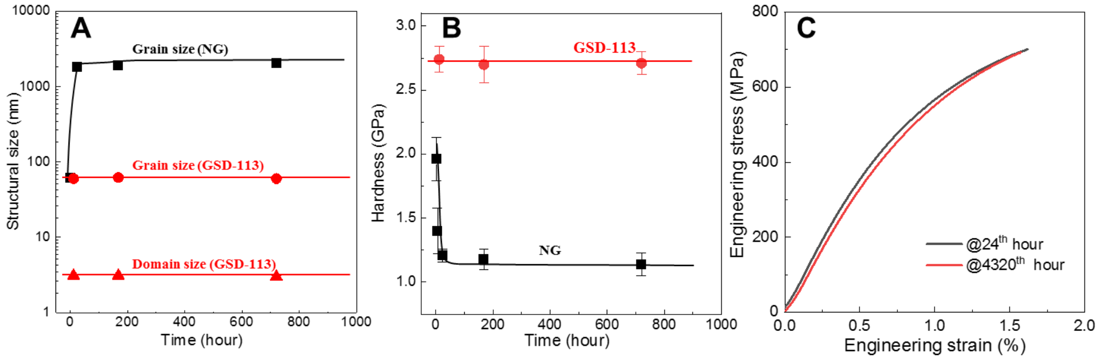

Fig. S7 Microstructural and mechanical stability as a function of duration. (A) Temporal evolution of grain size and domain size in the GSD-113 sample. The grain size variation of a conventional NG Cu foil is plotted for comparison. (B) Time-dependent hardness evolution of the GSD Cu foil and the conventional NG foil. (C) Engineering tensile stress–strain curves of RD Cu foils after 24 h and 4320 h (180 days) of duration.

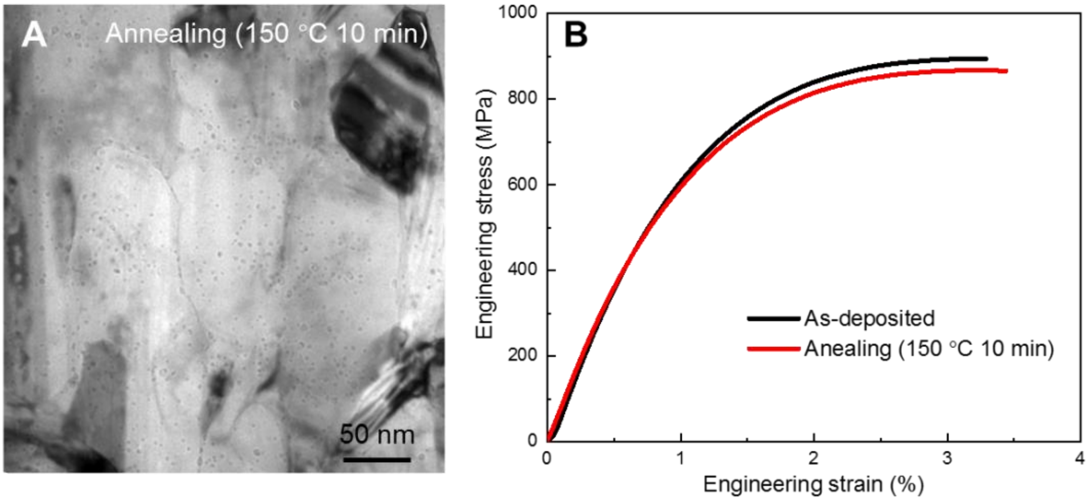

Fig. S8 GSD-113 annealed at 150 °C for 10 mins retains nearly the same microstructure (A) and tensile strength (B) as the as-prepared sample.

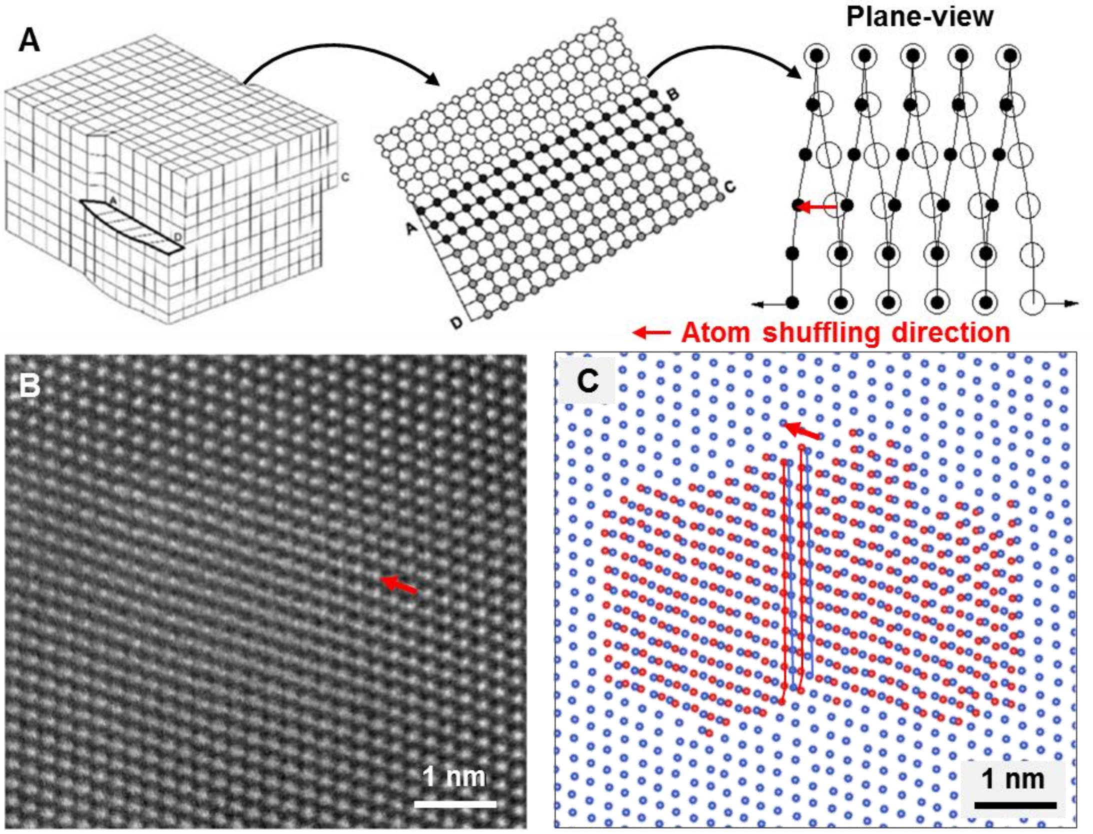

Fig. S9 (A) Schematic 3D and plan-view models of a screw dislocation, illustrating atomic shuffling parallel to the Burgers vector that forms zigzag atomic columns (red arrow; magnified at right) (*54, 55*). (B) Experimental HAADF image of the GSD sample showing a representative screw dislocation in plan view, with resolved atomic shuffling along the red arrow. (C) Atomic positions extracted from (B), showing normal (blue) and shuffled (red) atoms, consistent with the characteristic zigzag configuration of a screw dislocation.

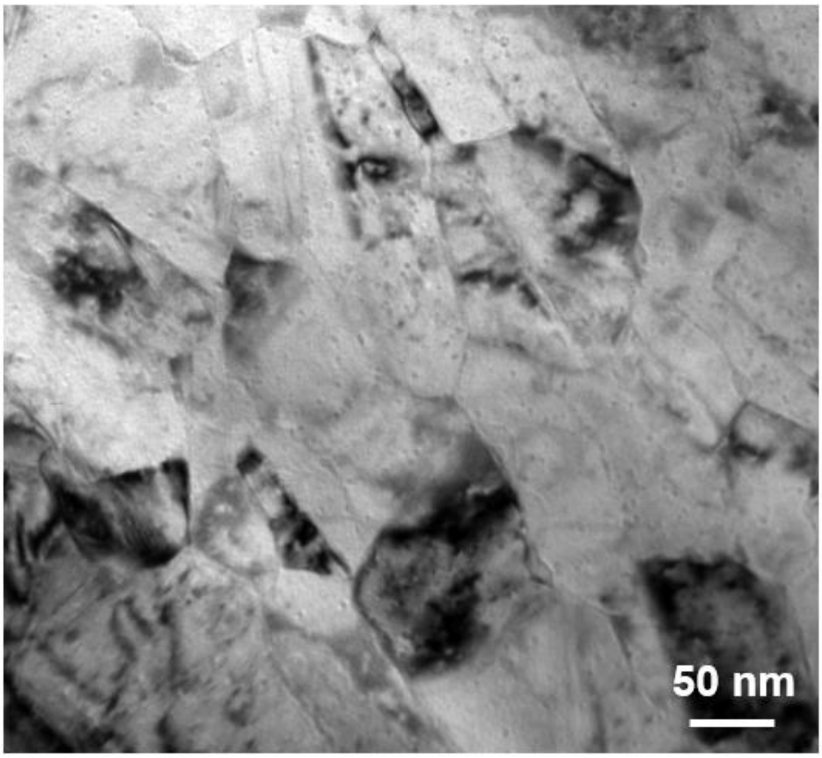

Fig. S10 Cross-sectional TEM image of an RD Cu foil, displaying a low density of dislocations activated after fracture.

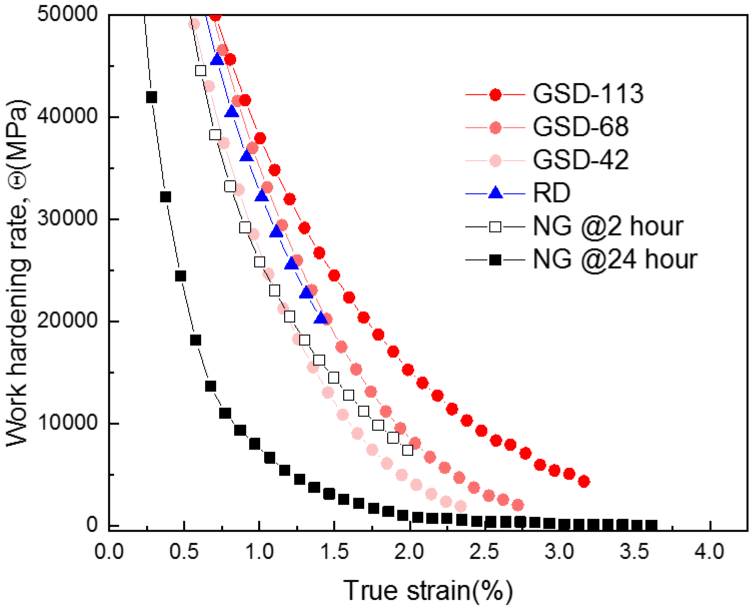

Fig. S11 Work-hardening rate versus true strain curves of GSD and RD Cu foils 24 hours after preparation, compared with those of NG Cu foils after 2 and 24 hours.

Table S1 Chemical composition of the as-deposited GSD-113 measured by glow discharge mass spectrometer. The average values were obtained by two independent measurements, and only elements with concentration above 0.1 ppm are listed**.**

Element	Content (ppm)		
	Measurement 1	Measurement 2	Average
C	190	210	200
N	138	134	136
S	12	4	8
O	229	250	240
Cl	321	296	309
K	8	12	10
Ti	1.2	1.2	1.2
Cr	0.2	0.3	0.25

References and notes

1. M. Wu, Z. Zhang, X. Xu, Z. Zhang, Y. Duan, J. Dong, R. Qiao, S. You, L. Wang, J. Qi, D. Zou, N. Shang, Y. Yang, H. Li, L. Zhu, J. Sun, H. Yu, P. Gao, X. Bai, Y. Jiang, Z.-J. Wang, F. Ding, D. Yu, E. Wang, K. Liu, Seeded growth of large single-crystal copper foils with high-index facets. *Nature* **581**, 406–410 (2020). doi:10.1038/s41586-020-2298-5 Medline

2. H. Y. Hsiao, C.-M. Liu, H. W. Lin, T.-C. Liu, C.-L. Lu, Y.-S. Huang, C. Chen, K. N. Tu, Unidirectional growth of microbumps on (111)-oriented and nanotwinned copper. *Science* **336**, 1007–1010 (2012). doi:10.1126/science.1216511 Medline

3. Z. Zhang, Y. Song, B. Zhang, L. Wang, X. He, Metallized plastic foils: A promising solution for high-energy lithium-ion battery current collectors. *Adv. Energy Mater.* **13**, 2302134 (2023). doi:10.1002/aenm.202302134

4. M. A. Meyers, A. Mishra, D. J. Benson, Mechanical properties of nanocrystalline materials. *Prog. Mater. Sci.* **51**, 427–556 (2006). doi:10.1016/j.pmatsci.2005.08.003

5. K. Yang, Y. Wang, M. Guo, H. Wang, Y. Mo, X. Dong, H. Lou, Recent development of advanced precipitation-strengthened Cu alloys with high strength and conductivity: A review. *Prog. Mater. Sci.* **138**, 101141 (2023). doi:10.1016/j.pmatsci.2023.101141

6. S. Z. Han, E. A. Choi, S. H. Lim, S. Kim, J. Lee, Alloy design strategies to increase strength and its trade-offs together. *Prog. Mater. Sci.* **117**, 100720 (2021). doi:10.1016/j.pmatsci.2020.100720

7. C. Liu, X. Chen, Z. Cheng, L. Lu, The effect of 2-mercaptobenzimidazole concentration on the microstructure and mechanical properties of electrodeposited Cu foils. *Electrochim. Acta* **531**, 146330 (2025). doi:10.1016/j.electacta.2025.146330

8. Y. Sun, L. Huang, H. Xie, B. Liu, Y. Fang, G. Han, J. Liu, High-strength copper foil prepared with 2-mercaptothiazoline by direct current electrodeposition. *Electrochim. Acta* **466**, 143068 (2023). doi:10.1016/j.electacta.2023.143068

9. L. L. Lu, H.-T. Liu, Z.-D. Wang, Q.-Q. Lu, Y.-J. Zhou, F. Zhou, Y.-M. Zhang, W.-W. Lu, B. Yang, Q.-Q. Zhu, K.-X. Song, Advances in electrolytic copper foils: Fabrication, microstructure, and mechanical properties. *Rare Met.* **44**, 757–792 (2025). doi:10.1007/s12598-024-02965-6

10. P. Broekmann, A. Fluegel, C. Emnet, M. Arnold, C. Roeger-Goepfert, A. Wagner, N. T. M. Hai, D. Mayer, Classification of suppressor additives based on synergistic and antagonistic ensemble effects. *Electrochim. Acta* **56**, 4724–4734 (2011). doi:10.1016/j.electacta.2011.03.015

11. P. Xu, W. Lu, K. Song, H. Cheng, H. Hu, Q. Zhu, H. Liu, X. Yang, Preparation of electrodeposited copper foils with ultrahigh tensile strength and elongation: A

functionalized ionic liquid as the unique additive. *Chem. Eng. J.* **484**, 149557 (2024). doi:10.1016/j.cej.2024.149557

12. J. Schiøtz, K. W. Jacobsen, A maximum in the strength of nanocrystalline copper. *Science* **301**, 1357–1359 (2003). doi:10.1126/science.1086636 Medline
13. Z. C. Cordero, B. E. Knight, C. A. Schuh, Six decades of the Hall–Petch effect – a survey of grain-size strengthening studies on pure metals. *Int. Mater. Rev.* **61**, 495–512 (2016). doi:10.1080/09506608.2016.1191808
14. A. F. Mayadas, M. Shatzkes, Electrical-resistivity model for polycrystalline films: The case of arbitrary reflection at external surfaces. *Phys. Rev., B, Solid State* **1**, 1382–1389 (1970). doi:10.1103/PhysRevB.1.1382
15. J. M. E. Harper, C. Cabral Jr., P. C. Andricacos, L. Gignac, I. C. Noyan, K. P. Rodbell, C. K. Hu, Mechanisms for microstructure evolution in electroplated copper thin films near room temperature. *J. Appl. Phys.* **86**, 2516–2525 (1999). doi:10.1063/1.371086
16. K. Lu, Stabilizing nanostructures in metals using grain and twin boundary architectures. *Nat. Rev. Mater.* **1**, 16019 (2016). doi:10.1038/natrevmats.2016.19
17. L. Lu, Y. Shen, X. Chen, L. Qian, K. Lu, Ultrahigh strength and high electrical conductivity in copper. *Science* **304**, 422–426 (2004). doi:10.1126/science.1092905 Medline
18. D. P. Tran, K.-J. Chen, K. N. Tu, C. Chen, Y.-T. Chen, S. Chung, Electrodeposition of slanted nanotwinned Cu foils with high strength and ductility. *Electrochim. Acta* **389**, 138640 (2021). doi:10.1016/j.electacta.2021.138640
19. Z. Cheng, H. Zhou, Q. Lu, H. Gao, L. Lu, Extra strengthening and work hardening in gradient nanotwinned metals. *Science* **362**, eaau1925 (2018). doi:10.1126/science.aau1925 Medline
20. I. Matsui, T. Uesugi, Y. Takigawa, K. Higashi, Effect of interstitial carbon on the mechanical properties of electrodeposited bulk nanocrystalline Ni. *Acta Mater.* **61**, 3360–3369 (2013). doi:10.1016/j.actamat.2013.02.025
21. Q. Huang, Effects of impurity elements on isothermal grain growth of electroplated copper. *J. Electrochem. Soc.* **165**, D251–D257 (2018). doi:10.1149/2.0271807jes
22. C. Dai, Z. Wang, K. Liu, X. Zhu, X. Liao, X. Chen, Y. Pan, Effects of cycle times and C-rate on mechanical properties of copper foil and adhesive strength of electrodes in commercial $LiCoO_2$ LIBs. *Eng. Fail. Anal.* **101**, 193–205 (2019). doi:10.1016/j.engfailanal.2019.03.015
23. Z. Dong, X. Fei, L. Feng, J. Nie, W. Li, B. Gong, Effects of deformation and applied temperature on the microstructure and performance of industrial ultra-

thin rolled Cu foil. *J. Mater. Res. Technol.* **23**, 4268–4279 (2023). doi:10.1016/j.jmrt.2023.02.084

24. X. Q. Yin, L.-J. Peng, S. Kayani, L. Cheng, J.-W. Wang, W. Xiao, L.-G. Wang, G.-J. Huang, Mechanical properties and microstructure of rolled and electrodeposited thin copper foil. *Rare Met.* **35**, 909–914 (2016). doi:10.1007/s12598-016-0806-4
25. Z. G. Li, L. Y. Gao, Z. Li, R. Sun, Z. Q. Liu, Regulating the orientation and distribution of nanotwins by trace of gelatin during direct current electroplating copper on titanium substrate. *J. Mater. Sci.* **57**, 17797–17811 (2022). doi:10.1007/s10853-022-07731-6
26. J. Zhu, J. Feng, Z. Guo, Mechanical properties of commercial copper current-collector foils. *RSC Adv.* **4**, 57671–57678 (2014). doi:10.1039/C4RA07675C
27. K. P. Lee, B.-Y. Chen, Y.-Q. Lin, Y.-W. Hung, W.-Y. Hsu, Y.-H. Chen, C. Chen, High-strength and high-conductivity nanotwinned Cu lightly doped with Ni. *Mater. Sci. Eng. A* **891**, 145990 (2024). doi:10.1016/j.msea.2023.145990
28. Y. Zhang, Y. S. Li, N. R. Tao, K. Lu, High strength and high electrical conductivity in bulk nanograined Cu embedded with nanoscale twins. *Appl. Phys. Lett.* **91**, 211901 (2007). doi:10.1063/1.2816126
29. R. Feng, W. Zhao, Y. Sun, X. Wang, B. Gong, B. Chang, T. Feng, Softened microstructure and properties of 12 μm thick rolled copper foil. *Materials* **15**, 2249 (2022). doi:10.3390/ma15062249 Medline
30. X. Ma, C. Huang, J. Moering, M. Ruppert, H. W. Höppel, M. Göken, J. Narayan, Y. Zhu, Mechanical properties of copper/bronze laminates: Role of interfaces. *Acta Mater.* **116**, 43–52 (2016). doi:10.1016/j.actamat.2016.06.023
31. T. Ungár, E. Schafler, P. Hanák, S. Bernstorff, M. Zehetbauer, Vacancy production during plastic deformation in copper determined by in situ X-ray diffraction. *Mater. Sci. Eng. A* **462**, 398–401 (2007). doi:10.1016/j.msea.2006.03.156
32. D. A. Hughes, N. Hansen, The microstructural origin of work hardening stages. *Acta Mater.* **148**, 374–383 (2018). doi:10.1016/j.actamat.2018.02.002
33. U. Essmann, H. Mughrabi, Annihilation of dislocations during tensile and cyclic deformation and limits of dislocation densities. *Philos. Mag. A Phys. Condens. Matter Defects Mech. Prop.* **40**, 731–756 (1979). doi:10.1080/01418617908234871
34. C. C. Koch, D. G. Morris, K. Lu, A. Inoue, Ductility of nanostructured materials. *MRS Bull.* **24**, 54–58 (1999). doi:10.1557/S0883769400051551
35. F. Wang, M. Song, M. N. Elkot, N. Yao, B. Sun, M. Song, Z. Wang, D. Raabe, Shearing brittle intermetallics enhances cryogenic strength and ductility of steels. *Science* **384**, 1017–1022 (2024). doi:10.1126/science.ado2919 Medline
36. S. Jiang, H. Wang, Y. Wu, X. Liu, H. Chen, M. Yao, B. Gault, D. Ponge, D. Raabe, A. Hirata, M. Chen, Y. Wang, Z. Lu, Ultrastrong steel via minimal lattice misfit

and high-density nanoprecipitation. *Nature* **544**, 460–464 (2017). doi:10.1038/nature22032 Medline

37. W. Sun, Y. Zhu, R. Marceau, L. Wang, Q. Zhang, X. Gao, C. Hutchinson, Precipitation strengthening of aluminum alloys by room-temperature cyclic plasticity. *Science* **363**, 972–975 (2019). doi:10.1126/science.aav7086 Medline
38. X. Wu, F. Yuan, M. Yang, P. Jiang, C. Zhang, L. Chen, Y. Wei, E. Ma, Nanodomained nickel unite nanocrystal strength with coarse-grain ductility. *Sci. Rep.* **5**, 11728 (2015). doi:10.1038/srep11728 Medline
39. G. Wu, K. C. Chan, L. Zhu, L. Sun, J. Lu, Dual-phase nanostructuring as a route to high-strength magnesium alloys. *Nature* **545**, 80–83 (2017). doi:10.1038/nature21691 Medline
40. M. Yamaguchi, M. Shiga, H. Kaburaki, Grain boundary decohesion by impurity segregation in a nickel-sulfur system. *Science* **307**, 393–397 (2005). doi:10.1126/science.1104624 Medline
41. Z. Li, Y. Zhang, Z. Zhang, Y.-T. Cui, Q. Guo, P. Liu, S. Jin, G. Sha, K. Ding, Z. Li, T. Fan, H. M. Urbassek, Q. Yu, T. Zhu, D. Zhang, Y. M. Wang, A nanodispersion-in-nanograins strategy for ultra-strong, ductile and stable metal nanocomposites. *Nat. Commun.* **13**, 5581 (2022). doi:10.1038/s41467-022-33261-5 Medline
42. W. Huang, Oxide nanocrystal model catalysts. *Acc. Chem. Res.* **49**, 520–527 (2016). doi:10.1021/acs.accounts.5b00537 Medline
43. K. Chang, W. Feng, L. Q. Chen, Effect of second-phase particle morphology on grain growth kinetics. *Acta Mater.* **57**, 5229–5236 (2009). doi:10.1016/j.actamat.2009.07.025
44. T. H. Fang, W. L. Li, N. R. Tao, K. Lu, Revealing extraordinary intrinsic tensile plasticity in gradient nano-grained copper. *Science* **331**, 1587–1590 (2011). doi:10.1126/science.1200177 Medline
45. Q. Pan, L. Zhang, R. Feng, Q. Lu, K. An, A. C. Chuang, J. D. Poplawsky, P. K. Liaw, L. Lu, Gradient cell-structured high-entropy alloy with exceptional strength and ductility. *Science* **374**, 984–989 (2021). doi:10.1126/science.abj8114 Medline
46. M. Göken, H. W. Höppel, Tailoring nanostructured, graded, and particle-reinforced Al laminates by accumulative roll bonding. *Adv. Mater.* **23**, 2663–2668 (2011). doi:10.1002/adma.201100407 Medline
47. L. Liu, C. Liu, J. Zheng, Z. Cheng, L. Lu, Unit-level hardening-driven strengthening in gradient nanotwinned Cu. *Scr. Mater.* **271**, 116973 (2026). doi:10.1016/j.scriptamat.2025.116973
48. H. Gao, Y. Huang, W. D. Nix, J. W. Hutchinson, Mechanism based strain gradient plasticity-I. Theory. *J. Mech. Phys. Solids* **47**, 1239–1263 (1999). doi:10.1016/S0022-5096(98)00103-3

49. J. P. Hirth, J. Lothe, *Theory of Dislocations* (Wiley, ed. 2, 1982).

50. U. F. Kocks, H. Mecking, Physics and phenomenology of strain hardening: The FCC case. *Prog. Mater. Sci.* **48**, 171–273 (2003). doi:10.1016/S0079-6425(02)00003-8

51. H. Chen, K. Chen, Y. Sheng, J. Qu, X. Wang, D. You, D. Shan, Properties and microstructure regulation of electrodeposited ultra-thin copper foil in a simple additive system. *Mater. Res. Express* **11**, 056405 (2024). doi:10.1088/2053-1591/ad4e9e

52. T. Chang, Y. Jin, L. Wen, C. Zhang, C. Leygraf, I. O. Wallinder, J. Zhang, Synergistic effects of gelatin and convection on copper foil electrodeposition. *Electrochim. Acta* **211**, 245–254 (2016). doi:10.1016/j.electacta.2016.06.051

53. P. J. Phillips, M. C. Brandes, M. J. Mills, M. De Graef, Diffraction contrast STEM of dislocations: Imaging and simulations. *Ultramicroscopy* **111**, 1483–1487 (2011). doi:10.1016/j.ultramic.2011.07.001 Medline

54. M. T. Dove, *Structure and Dynamics: An Atomic View of Materials* (Oxford Univ. Press, 2003).

55. A. H. Cottrell, *Dislocations and Plastic Flow in Crystals* (Oxford Univ. Press, 1953).

Acknowledgments

We thank X. C. Chen for help with sample preparation.

Funding: L. Lu acknowledges financial support from the National Natural Science Foundation of China (NSFC grants 92463302 and U24A2027), the project of Global Common Challenges (grant 172GJHZ2023075GC), and the Chinese Academy of Sciences (CAS). Z.C. acknowledges financial support from the NSFC (grants 52422102 and 52371124), the National Key R&D Program of China (grant 2024YFA1210600), and the Youth Innovation Promotion Association of CAS. Z.Y. acknowledges financial support from the NSFC (grant 52222102).

Author contributions: L. Lu initiated and supervised the project. Z.C. and L. Liu prepared the sample, performed the experimental tests, and conducted SEM observations. Z.Y. and X.Y. conducted TEM observations. Z.C. and L. Lu designed the experiments and drafted the manuscript. All authors contributed to the discussions and revised the manuscript.

Competing interests: The authors declare no competing interests.

Data, code, and materials availability: All data generated or analyzed during this study are included in the main text or the supplementary materials. All raw materials used in the virgin make-up solution and additives were purchased from Sinopharm Chemical Reagent Co., Ltd.

Supplementary Materials

science.org/doi/10.1126/science.aed7758

Materials and Methods

Figs. S1 to S11

Table S1

References (*51–55*)

Submitted 10 November 2025; accepted 9 February 2026

Fig. 1. Microstructure and chemistry of GSD Cu foils. (**A**) Cross-sectional SEM image. Inset shows a higher-magnification SEM image and the corresponding secondary ion mass spectrometry (SIMS) profiles with the distributions of C, O, and Cl along the depth. The growth direction is indicated by a white arrow. (**B**) Cross-sectional TEM image revealing periodically distributed GSDs. (**C**) Enlarged TEM image showing neighboring layers I and II. The inset shows the atomic structure of layer I. (**D**) TEM tomography reconstruction showing the 3D distribution of domains. The GBs of NGs are outlined. Both domains and GBs collectively constitute the GSD Cu microstructure. The x, y, and z axes correspond to the length (tensile), width, and thickness directions of the Cu foil, respectively. (**E**) Variation of domain volume fraction (f) along the depth. (**F** to **L**) Characterizations of a single domain in layer II through ADF imaging (F), iDPC analysis (G), GPA analysis (H), experimentally extracted atomic strain map (I), and electron energy loss spectroscopy maps of Cu (J), C (K), and O (L). Panels (F) to (I) and panels (J) and (L) share the same scale bars.

Fig. 2. Mechanical and electrical properties of GSD Cu foils. (**A**) Engineering tensile stress-strain curves of GSD-42, GSD-68, and GSD-113 compared with RD Cu foil after 24 hours of processing. (**B**) Long-term mechanical stability of GSD-113 showing its tensile behavior after 4320 hours (180 days) compared with NG Cu foils after 2 and 24 hours. Schematic illustrations in the insets depict the characteristic microstructural configurations for GSD, RD, and NG Cu foils. (**C** and **D**) Comparison of ultimate tensile strength versus elongation (C) and electrical conductivity (D) of GSD Cu foils with those of RD Cu foils, conventional Cu foils (*7*, *8*, *22–26*), and Cu alloys (*27–29*).

Fig. 3. Deformed microstructure of GSD-113. (**A**) Cross-sectional SEM image near the fracture region. (**B** and **C**) HAADF and BF images revealing the distribution of domains and dislocations. (**D**) Schematic illustration showing the superposition of domains and dislocations derived from (B) and (C), where domains, long dislocations in layer I, and short dislocations in layer II are outlined in red, orange, and blue,

respectively. (B) to (D) share the same scale bar. (**E** and **F**) HAADF and BF images showing long dislocations pinned by domains between layers I and II. (**G**) Magnified iDPC image of the region marked by the box in (D), including a long dislocation. Insets in (G) display the atomic structures of the sheared (left) and unsheared (right) regions, with the Burgers vector indicated by an arrow.

Fig. 4. Dislocation behavior in layer II of GSD-113. (**A**) Atomistic iDPC-STEM image showing high-density short dislocation segments (blue circles) distributed around super-nano domains (dotted circles). Edge dislocations and stacking faults are indicated by white ⊥ symbols and polylines, respectively. (**B**) Magnified view showing short dislocation segments. (**C** and **D**) Atomic-resolution image and corresponding reconstructed atomic model of a representative short dislocation segment, confirming its predominant screw character. (**E** and **F**) HAADF image and GPA strain map of layer II enriched with super-nano domains. The color contour represents the distribution of atomic strain (ε_{xx}).

Table 1. Microstructure characteristic length and tensile properties of GSD, RD, and conventional NG Cu foils.

Cu foil	d_G **(nm)**	d_D **(nm)**	S **(%/µm)**	f **(%)**	σ_{uts} **(MPa)**	δ_f **(%)**
GSD-113	60 ± 3	3.0 ± 0.1	113	3.2	889 ± 6	3.2 ± 0.3
GSD-68	71 ± 3	3.3 ± 0.1	68	1.7	761 ± 27	2.9 ± 0.2
GSD-42	80 ± 2	3.1 ± 0.1	42	1.0	688 ± 33	2.8 ± 0.3
RD	77 ± 2	3.4 ± 0.1	—	1.5	701 ± 12	1.8 ± 0.1
NG	61 ± 2	—	—	—	630 ± 27	2.4 ± 0.2

d_G**,** grain size; d_D, domain size; S, structural gradient; f, overall volume fraction of domains; σ_{uts}, ultimate tensile strength; δ_f, elongation